

# Different Nucleation Mechanisms during Atomic Layer Deposition of HfS<sub>2</sub> on Cobalt Oxide Surfaces

Georg Fickenscher<sup>1</sup>, Nikolai Sidorenko<sup>1</sup>, Kira Mikulinskaya<sup>1</sup>, Jörg Libuda<sup>1\*</sup>

<sup>1</sup> *Interface Research and Catalysis, ECRC, Friedrich-Alexander-Universität Erlangen-Nürnberg, Egerlandstraße 3, 91058 Erlangen, Germany*

\*corresponding author: Jörg Libuda, joerg.libuda@fau.de

## Abstract

We investigated the atomic layer deposition (ALD) of HfS<sub>2</sub> on atomically defined CoO(100) and CoO(111) surfaces under ultrahigh-vacuum (UHV) conditions. The ALD process was performed by sequential dosing of the precursors tetrakis(dimethylamido)hafnium (TDMAH) and deuterium sulfide (D<sub>2</sub>S) separated by purging periods. The growth and nucleation reactions were monitored by in situ infrared reflection absorption spectroscopy (IRAS).

HfS<sub>2</sub> films nucleate and grow on both cobalt oxide surfaces, despite the fact that CoO(100) lacks acidic protons and CoO(111) exposes only very few OH groups at defects. On these OH-free or OH-lean surfaces, the nucleation step involves a Lewis acid-base reaction instead. The stoichiometry of the –Hf(NMe<sub>2</sub>)<sub>x</sub> nuclei changes during the first ALD half cycle. On CoO(100), the split-off ligands bind as –NMe<sub>2</sub> to surface cobalt ions. The nucleation on CoO(111) is more complex and the split-off ligands undergo dehydrogenation to form various surface species with C=N double and C≡N triple bonds and surface OH.

Our findings reveal a new nucleation mechanism for ALD in the absence of acidic protons and show that other factors such as Lewis acidity, surface structure, and surface reactivity must also be considered in the nucleation event.

**Keywords:** cobalt oxide, infrared reflection absorption spectroscopy, atomic layer deposition, HfS<sub>2</sub>, Lewis acid-base reaction

## 1. Introduction

In recent years, Atomic Layer Deposition (ALD) has become an extremely versatile and precise method for producing thin layers of a wide variety of materials on surfaces.<sup>1-11</sup> With its ability to conformally deposit materials of excellent quality layer-by-layer and with atomic precision<sup>12-</sup>

<sup>17</sup>, ALD enables a wide range of applications in microelectronics, nanotechnology, and catalysis.<sup>18-21</sup> In ALD, two reactive precursors are alternately dosed onto a substrate, resulting in self-terminating chemical reactions that lead to the formation of the desired thin film.<sup>20, 22-30</sup> The manufacturing of transition-metal dichalcogenides (TMDCs) semiconductors has been of particular interest lately due to their adjustable band gaps<sup>31-36</sup> and unique electronic and optoelectronic properties.<sup>37-41</sup> Among the TMDCs, HfS<sub>2</sub> has emerged as an excellent alternative to the well-known MoS<sub>2</sub>, as it has higher mobility while preserving a high on/off ratio and suitable bandgap.<sup>36, 42-47</sup>

The initial nucleation is probably the most decisive step in the production of ultrathin film of exceptional quality. To ensure defect-free production of miniaturized semiconductors, the nucleation must proceed uniformly to suppress island growth.<sup>2, 14</sup> ALD precursors react with a substrate using defects or functional groups on a surface as nucleation sites.<sup>2</sup> Typical surface functional groups that enable ALD growth exhibit acidic protons, e.g. –H, –OH, –COOH, –SH, and –NH<sub>2</sub>.<sup>36, 48-55</sup> In contrast, surfaces without such a functionalization have been shown to be ALD-inactive.<sup>2, 52, 56-59</sup> In two recent studies we have investigated the ALD of HfS<sub>2</sub> on hydroxylated Co<sub>3</sub>O<sub>4</sub>(111)<sup>53</sup> and on Co<sub>3</sub>O<sub>4</sub>(111) covered by –OH functionalized and non-functionalized self-assembled monolayers (SAMs).<sup>52</sup> We could show that the presence of acidic protons is essential for the ALD process to proceed.

In this work, we report on the results of a surface science model study investigating the initial nucleation and growth of HfS<sub>2</sub> by ALD on pristine cobalt oxide surfaces. In particular, we scrutinize the formation of Hf nuclei and by-products from TDMAH on atomically defined CoO(100) and CoO(111) films grown on Ir(100). The structures of CoO(100) and CoO(111) films as well as the adsorption of water on these surfaces have been investigated in detail previously.<sup>60-64</sup> Here, we present the results of an in situ IRAS study in which we explore the chemical reactions and surface species that appear during the initial nucleation step, i.e. during the first half cycle of the ALD procedure. We demonstrate that the nucleation of TDMAH on CoO(100) and CoO(111) does not require surface OH groups or protons but can proceed through a Lewis acid-base reaction as well. We further demonstrate that the nucleation process can also involve complex reactions on the surface, including changes in the stoichiometry of Hf nuclei, redox processes, and dehydrogenation reactions. These surface reactions heavily dependent on the structure and chemical properties of the substrate at the atomic scale.

## 2. Experimental Section

All experiments were performed using a UHV apparatus (base pressure of  $2.0 \times 10^{-10}$  mbar) for surface science studies at the Friedrich-Alexander-Universität Erlangen-Nürnberg, Germany. The apparatus is equipped with an FTIR spectrometer (Bruker VERTEX 80v) and a liquid nitrogen-cooled mercury cadmium telluride (LN-MCT) detector. The spectrometer and detector are connected to the UHV chamber on opposing sides via differentially pumped KBr windows. The ALD experiments were conducted in a remote-controlled manner using a LabView (National Instruments) interface. This enables precise control of the heating, measuring, and dosing processes as well as their synchronization. A schematic of the setup is depicted in Figure 1a.

#### *Chemicals.*

Tetrakis(dimethylamido)hafnium (TDMAH; 98+%; 99.99+% Hf; <0.2% Zr) was ordered from Strem. Deuterated hydrogen sulfide ( $D_2S$ ; 97 atom % D) was purchased from Sigma-Aldrich.

#### *Preparation of CoO(111)/Ir(100).*

The CoO(111) thin films were prepared on an Ir(100) surface via physical vapor deposition (PVD) of cobalt metal in a reactive  $O_2$  atmosphere. Prior to the deposition, the Ir(100) surface was cleaned by sputtering with  $Ar^+$  ions (2 x 45 min,  $p(Ar) = 5.0 \times 10^{-5}$  mbar,  $E_{kin}(Ar^+) = 1.80$  keV,  $I_{ion} = 50 \mu A$ ; Linde, 6.0). Subsequently, the sample was annealed at 1093 K for 10 min in UHV. Following an adapted procedure developed by Heinz et al.<sup>60, 65</sup>, the sample was further annealed at 1093 K for 10 min in  $5 \times 10^{-8}$  mbar  $O_2$  (Linde, 5.0) and then cooled to below 423 K while maintaining the  $O_2$  atmosphere. This resulted in a Ir(100)-(2x1)O structure as verified by low energy electron diffraction (LEED). Subsequently,  $Co_3O_4(111)$  thin films were prepared by evaporating cobalt (2 mm rod, Alfa Aesar, 99.95%) onto the surface using an electron beam evaporator (Focus EFM3,  $I_{Fil} = 2.75$  A,  $U_{HV} = 950$  V,  $I_{Em} = 11$  mA,  $I_{ion} = 30$  nA, 20 min) in  $9.5 \times 10^{-6}$  mbar  $O_2$  at a sample temperature of 293 K. After deposition, the sample was post-annealed in four consecutive steps: At 548 K (i) in  $5 \times 10^{-7}$  mbar  $O_2$  for 3 min and (ii) in UHV for 2 min, then at 693 K (iii) in  $5 \times 10^{-8}$  mbar  $O_2$  for 20 min and finally (iv) in UHV for 5 min. The quality of the resulting  $Co_3O_4(111)$  surface was verified using LEED. Finally, the  $Co_3O_4(111)$  film was transformed into CoO(111) by annealing at 893 K for 5 min in UHV. The quality of the CoO(111) film was again checked by LEED. A ball model of the surface structure is provided in Figure 1c.

#### *Preparation of CoO(100)/CoIr(100).*

For the preparation of CoO(100) films, Ir(100) was first cleaned and transformed into a Ir(100)-(2x1)O structure (as described above). Afterwards, the sample was annealed in  $2 \times 10^{-7}$  mbar  $H_2$  (Linde, 5.3) at 533 K for 1 min and then at the same temperature in UHV for 1 min. This

resulted in a metastable Ir(100)-(1×1) reconstructed surface. Next, a thin layer of metallic cobalt was deposited on the surface ( $I_{\text{Fil}} = 2.75$  A,  $U_{\text{HV}} = 950$  V,  $I_{\text{Em}} = 11$  mA,  $I_{\text{ion}} = 30$  nA, 6 min) in UHV at a sample temperature of 343 K. After cooling the sample to below 193 K, cobalt was then deposited in a reactive oxygen atmosphere ( $7 \times 10^{-7}$  mbar) for 3 min. Subsequently, the sample was annealed at 373 K for 3 min in UHV to obtain a thin ordered CoO(100) structure. After cooling to below 223 K, a thicker and better-ordered CoO(100) film was prepared by further reactive deposition of cobalt in O<sub>2</sub> ( $7 \times 10^{-7}$  mbar) for 18 min. Finally, the CoO(100) film was annealed at 1073 K for 5 min. The quality of the resulting CoO(100) surface was verified by a sharp (1×1) LEED pattern. A ball model of the surface structure is depicted in Figure 1b.

*IRAS of ALD on CoO(100)/Co/Ir(100) and CoO(111)/Ir(100) at 400 K.*

Prior to starting the ALD procedure, a 10 min IR background spectrum was recorded. Subsequently, 10 ALD cycles were performed by consecutive dosing of TDMAH and D<sub>2</sub>S via electromagnetic valves. In every ALD cycle, TDMAH was first dosed continuously over a course of 5 min with a duty cycle of 0.0085 (opening time 125 ms per 15 s dosing, pressure was always below  $5 \times 10^{-6}$  mbar) (i), followed by 2 min of pumping (ii), dosing D<sub>2</sub>S ( $1 \times 10^{-6}$  mbar) over a course of 10 min (iii), and finally 2 min of pumping (iv). TDMAH was dosed from the vapor phase above the neat compound in a glass crucible at room temperature (vapor pressure is 0.1 Torr at 48°C, Strem) and D<sub>2</sub>S was dosed from a gas reservoir ( $p(\text{D}_2\text{S}) = 1$  mbar). Each ALD cycle (steps (i) to (iv)) was completed in 19 min. Recording of IR spectra and gas dosing was synchronized using LabView. Accordingly, 19 spectra with an acquisition time of 1 min were recorded during each ALD cycle.

*IRAS of TDMAH on pristine CoO(100)/Co/Ir(100) and CoO(111)/Ir(100) at 400 K.*

For the in-situ IRAS experiments regarding the first ALD half cycle on the pristine cobalt oxides, we first recorded a 10 min IR background spectrum. Next, we exposed the sample to very small amounts of TDMAH by applying short gas pulses (opening time of the electromagnetic valve: 50x 10 ms, then 10x 25 ms, finally 10x 50 ms pulses on CoO(100); 50x 15 ms pulses, then 10x 25 ms, finally 10x 50 ms pulses on CoO(111)). As a result, we obtained a very low TDMAH dose per pulse, which allowed us to decouple the measurement time from the exposure. After each pulse of TDMAH, we recorded a 1 min IR spectrum.

### 3. Results and Discussion

#### 3.1. ALD of HfS<sub>2</sub> on CoO(100) at 400 K.

In the first step, we performed an ALD experiment on CoO(100) at 400 K under UHV conditions. Previously, Heinz et al. investigated the structure and properties of cobalt oxides grown on Ir(100) using LEED, scanning tunneling microscopy (STM), and density functional theory (DFT).<sup>60-62, 65</sup> They found that CoO(100) is non-polar and exhibits a bulk-like termination with oxygen and cobalt ions in the same plane.<sup>60</sup> Water adsorbs molecularly on CoO(100) below 210 K, exposing only very few OH groups at defect sites that completely disappear from the surface above 360 K.<sup>63-64</sup> We chose the reaction temperature at 400 K based on previous studies that have shown that the reactions of the ALD process are most efficient at this temperature.<sup>36</sup> Additionally, at 400 K, the CoO(100) surface does not exhibit acidic protons.<sup>63-64</sup> In total, we performed 10 full ALD cycles, each consisting of 4 steps, i.e., (i) dosing TDMAH for 5 min, (ii) pumping for 2 min, (iii) dosing D<sub>2</sub>S for 10 min, and finally (iv) pumping for 2 min. While performing ALD, we continuously recorded IR spectra (1 min per spectrum, 19 spectra every full ALD cycle). The recorded set of IR spectra is shown as difference spectra (spectrum(n) – spectrum(n–1)) in Figure 2a. By referencing against the previous spectrum, negative IR bands indicate the adsorption of a species, while positive IR bands indicate the loss or consumption of a species.

The total set of IR spectra is shown in Figure 2a. The integrated CH area for each spectrum is depicted in Figure 2b. Starting with the adsorption of TDMAH, we observe negative bands (blue, adsorption) at 2872, 2856, 2820, 2771, 1239 and 948 cm<sup>-1</sup>. Additionally, less intense features appear at 1140 and 1060 cm<sup>-1</sup>, along with a broad band between 1410 and 1510 cm<sup>-1</sup>. The same features appear as positive bands (red, consumption) upon exposure to D<sub>2</sub>S. In later cycles, we observe a blueshift of several bands to 2872, 2830, 2780, between 1430 and 1485, 1254, 1140, 1060 and 954 cm<sup>-1</sup>. The integrated differential CH area plotted against the deposition time in Figure 2b reflects the approximate reaction rate and density of reactants (peak area, indicated as number next to each peak). In the first ALD cycle, we observe a larger peak area upon exposure to TDMAH and D<sub>2</sub>S than in later cycles. Comparing the peak shapes, we find sharper, more narrow bands during TDMAH exposure and broader, less intense bands during D<sub>2</sub>S exposure. Between signals, the differential CH area always decreases to zero.

The data presented is similar to previous in-situ IRAS studies investigating ALD of HfS<sub>2</sub> on Co<sub>3</sub>O<sub>4</sub>(111) that some of the authors have reported on before.<sup>36, 52-53</sup> We assign the appearance and loss of bands upon dosing of TDMAH and D<sub>2</sub>S, respectively, to the formation and loss of TDMAH-derived surface species. More specifically, the observed bands arise from surface-bound –NMe<sub>2</sub> ligands. For the band assignment, we refer to a study from Li et al. which provides a detailed description of the adsorption of TDMAH on hydrogen-terminated Si(100)<sup>55</sup>

using IR spectroscopy and DFT. In brief, the signals appearing at 2872, 2830 and 2780  $\text{cm}^{-1}$  are assigned to CH stretching vibrations  $\nu(\text{CH})$ , while the broad band appearing between 1430 and 1485  $\text{cm}^{-1}$  arises from CH deformation modes  $\delta(\text{CH})$ . The bands at 1254, 1140, and 1060  $\text{cm}^{-1}$  are assigned to coupled Hf–N, C–N, and C–H stretching and deformation modes. Finally, the signal at 954  $\text{cm}^{-1}$  is associated with coupled Hf–N–C stretching modes ( $\nu(\text{Hf–N})$  and  $\nu(\text{N–C})$ ). We conclude that the surface changes its termination reversibly during each ALD cycle. When exposed to TDMAH, the surface gradually becomes amine  $-\text{NMe}_2$  terminated due to the formation of TDMAH-derived surface species (appearance of signals). When exposed to  $\text{D}_2\text{S}$ , surface-bound  $-\text{NMe}_2$  species are converted into volatile  $\text{DNMe}_2$  species (loss of signals) and a thiol ( $-\text{SD}$ ) termination forms. The thiol-terminated surface can react with TDMAH again, enabling the next ALD cycle.

Next, we consider the peak shape and area of the integrated CH area over the course of 10 ALD cycles (Figure 2b). Despite the higher dose of  $\text{D}_2\text{S}$  during each cycle, the reaction with  $\text{D}_2\text{S}$  is slower than the reaction with TDMAH as shown by the broader and less intense peaks. However, both reactions are fast and self-terminate in less than 3 min. Interestingly, the bands in the first cycle are shifted with respect to those appearing in later cycles. Furthermore, the peak area in the first cycle differs drastically from later cycles for which it remains virtually constant. Firstly, this indicates that the surface is already completely and uniformly covered from cycle 2 onwards. Secondly, more  $-\text{NMe}_2$  species are formed upon nucleation in the first half cycle and are also lost in the second half cycle than in the subsequent ones.

In previous studies, we have investigated the nucleation of TDMAH on pristine  $\text{Co}_3\text{O}_4(111)$ <sup>53</sup> and on  $\text{Co}_3\text{O}_4(111)$  covered by functionalized (OH-terminated) and non-functionalized (hydrocarbon-terminated) self-assembled monolayers (SAMs).<sup>52</sup> In both studies, we found that the presence of OH groups, or more precisely acidic protons, is essential for nucleation. On the hydrocarbon-terminated SAM, nucleation and, thus, ALD of  $\text{HfS}_2$  were completely suppressed due to the lack of reactive nucleation sites.<sup>52</sup> Accordingly, one would expect no nucleation on  $\text{CoO}(100)$  due to the lack of acidic protons on the surface above 360 K.<sup>63-64</sup> However, the ALD process is not suppressed, but it proceeds homogeneously suggesting fast and efficient nucleation. In the following, we will scrutinize the first half cycle in more detail in order to identify how the nucleation proceeds on the  $\text{CoO}(100)$  surface.

### 3.2. TDMAH on pristine $\text{CoO}(100)$ at 400 K.

To investigate the processes and kinetics during the initial nucleation in more detail, we exposed the surface to very small amounts of TDMAH at 400 K. After each pulse, we recorded an IR

spectrum and referenced it against the background spectrum of the freshly prepared, pristine CoO(100). The corresponding set of spectra featuring the most prominent and characteristic<sup>55</sup> bands is shown in Figure 3a. The evolution of the integrated peak area for signals in the CH region and at around 1250 and 950  $\text{cm}^{-1}$  is given in Figure 3b.

We start by considering the CH region. Upon exposure to TDMAH, we immediately observe the formation of bands at 2861, 2818 and 2774  $\text{cm}^{-1}$ . The bands increase in intensity and gradually shift to higher wavenumbers. The two bands at higher wavenumbers shift to 2872 and 2830  $\text{cm}^{-1}$ , respectively. The band at lower wavenumber first shifts to 2767 and, finally, to 2779  $\text{cm}^{-1}$ . The integrated CH peak area increases with the number of pulses and eventually levels off after approximately 60 pulses. The signals at 1240 and 942  $\text{cm}^{-1}$  are also present from the first pulse onwards. Similar to the behavior in the CH region, both signals increase in intensity and gradually blueshift to 1253 and 954  $\text{cm}^{-1}$ , respectively. Looking at the evolution of the peak area, we observe that the peak area also increases for both signals upon initial exposure to TDMAH. After pulse 30, the peak area for the signal at 1240 – 1253  $\text{cm}^{-1}$  remains constant. In contrast, the peak area of the signal at 942 – 954  $\text{cm}^{-1}$  increases until it reaches its maximum after pulse 33 and then slightly decreases until saturation at the highest dose. Upon closer inspection, all signals originate from two overlapping bands that change their ratio over the course of the nucleation experiment, which is reflected as a shift.

As already discussed in Section 3.1, we observe the formation of TDMAH-derived surface species. The absence of acidic protons on CoO(100) at 400 K<sup>63-64</sup> and the fact that nucleation still takes place implies that TDMAH must react with CoO(100) via a different mechanism, i.e. not by splitting off  $-\text{NMe}_2$  ligands as volatile  $\text{HNMe}_2$ . In fact, the data suggests formation of two very similar but distinguishable ligand species. We propose that TDMAH reacts with CoO(100) in a Lewis acid-base reaction. As a result,  $-\text{Hf}(\text{NMe}_2)_x$  adsorbents are formed on surface oxygen (electron pair donor) and  $(4-x) -\text{NMe}_2$  adsorbents are formed on surface cobalt ions (electron pair acceptor) for each reacting TDMAH molecule. We base this hypothesis on two distinct observations. Firstly, we observe that the amount of TDMAH-derived surface species reacting in the first ALD cycle is larger than in later cycles (see Section 3.1). This is consistent with the idea that the  $-\text{NMe}_2$  ligands are not converted into volatile by-products but also bind to the surface in the first half cycle. Secondly, the described signals contain two overlapping bands, suggesting two very similar surface species. We tentatively assign the lower wavenumber components to  $-\text{NMe}_2$  ligands interacting with surface cobalt. As mentioned above, the  $-\text{Hf}(\text{NMe}_2)_x$  signals at around 1250 and 950  $\text{cm}^{-1}$  contain contributions from  $\nu(\text{Hf}-\text{N})$  stretching modes. As a result, we expect a slight shift for  $-\text{NMe}_2$  signals containing

contributions from  $\nu(\text{Co-N})$  stretching modes. Interestingly, the two components of each signal change their ratio until saturation. At low exposures, the cobalt-bound  $-\text{NMe}_2$  signals dominate the spectrum. At the highest exposure, the  $-\text{Hf}(\text{NMe}_2)_x$  signals dominate the spectrum. This indicates a change in stoichiometry over the course of the nucleation. Similar to the nucleation of TDMAH on pristine  $\text{Co}_3\text{O}_4(111)$ <sup>53</sup> and  $\text{Co}_3\text{O}_4(111)$  covered with 4'-hydroxy-4-biphenylcarboxylic acid<sup>52</sup>, we suggest that TDMAH loses more ligands at the beginning of the nucleation than at later stages. Accordingly, the number  $x$  of Hf bound ligands increases over the course of the experiment. Finally, we note that the slight decrease in peak area observed for the signal at around  $950\text{ cm}^{-1}$  indicates a reorientation of the surface species near saturation.

### 3.3. ALD of $\text{HfS}_2$ on $\text{CoO}(111)$ at 400 K.

In order to explore, whether the surface structure affects the nucleation process, we investigated ALD of  $\text{HfS}_2$  on a differently oriented cobalt oxide film, namely on  $\text{CoO}(111)$ .  $\text{CoO}(111)$  switches from a rocksalt-type to wurtzite-type stacking at the surface due to polarity compensation.<sup>60-61</sup> As a result,  $\text{CoO}(111)$  exhibits metallic character and is oxygen-terminated with cobalt ions located slightly below the surface.<sup>60</sup> Water does not adsorb in molecular form on  $\text{CoO}(111)$  but dissociates at a few defect sites forming strongly bound OH groups.<sup>64</sup> The ALD experiments on  $\text{CoO}(111)$  were performed under exactly the same conditions and with the same measurement procedures as on  $\text{CoO}(100)$  (see Section 3.1). The recorded set of IR spectra was again plotted in the form of difference spectra (spectrum( $n$ ) – spectrum( $n-1$ )). The corresponding data is shown in Figure 4a. The integrated area of the CH region for each spectrum is depicted in Figure 4b.

Upon exposure to TDMAH and  $\text{D}_2\text{S}$ , we again observe the characteristic bands for the ALD growth of  $\text{HfS}_2$  at 2873, 2829, 2780, 1485 – 1430, 1252, 1140, 1060 and  $952\text{ cm}^{-1}$ . The bands appear in every cycle and show no shift. The differential CH area plotted against deposition time again features negative and positive signals upon exposure to TDMAH and  $\text{D}_2\text{S}$ , respectively. The bands upon TDMAH exposure are again sharper and narrower while the bands upon  $\text{D}_2\text{S}$  exposure are again less intense and broader. Interestingly, we do not observe the distinct difference in peak area (number of reactants) from the first to later cycles as seen for  $\text{CoO}(100)$ . Most notably, the spectra in the first half cycle are very different from the rest. In particular, we observe several additional signals at 3676, 2188, 1630 – 1540, 1406, 1394, 1370 and  $1040\text{ cm}^{-1}$ .

Apparently,  $\text{HfS}_2$  nucleates and grows very efficiently on  $\text{CoO}(111)$  as well, as indicated by the appearance and disappearance of the characteristic signals (2873, 2829, 2780, 1485 – 1430,

1252, 1140, 1060 and 952  $\text{cm}^{-1}$ ). As for ALD of  $\text{HfS}_2$  on  $\text{CoO}(100)$ , the reaction with TDMAH is again faster than the reaction with  $\text{D}_2\text{S}$ . This is to be expected as only the reaction with the pristine substrate in the first half cycle should show a different behavior. The data further indicates that the surface is fully saturated from the first cycle on, as we do not observe any noticeable difference in peak area between cycles (Figure 4b). This suggests a homogeneous growth of  $\text{HfS}_2$  which is surprising considering the structure of  $\text{CoO}(111)$ . Taking into account that the  $\text{CoO}(111)$  is oxygen-terminated<sup>60</sup>, we would expect cobalt sites to be less accessible on  $\text{CoO}(111)$  than on  $\text{CoO}(100)$  which features oxygen and cobalt ions in the same plane.<sup>60</sup> However, we previously studied the reaction of carboxylic acids on  $\text{CoO}(111)$  and showed that carboxylate groups are formed and are able to bind to cobalt ions in the surface.<sup>66-71</sup> We concluded that the surface cobalt ions in  $\text{CoO}(111)$  (which are located only slightly below the surface oxygen ions) can rearrange to bind to an adsorbate species.. This observation suggests that also on the  $\text{CoO}(111)$  surface, Lewis acid sites are available for a reaction with the precursor.

A particularly interesting observation is the appearance of the signal at 3676  $\text{cm}^{-1}$  which we assign to surface OH groups. In a study by Schwarz et al.,<sup>64</sup> the interaction of water with atomically defined  $\text{CoO}(100)$ ,  $\text{CoO}(111)$  and  $\text{Co}_3\text{O}_4(111)$  was investigated. The authors showed that only very small amounts of OH groups are formed on  $\text{CoO}(111)$  at 400 K. These OH species were assigned to a small fraction of defect sites (for example at grain boundaries). Considering this information and the homogeneous growth from the first ALD cycle on, we exclude the possibility that the defect OH species are the primary nucleation sites for TDMAH in the first half cycle. Instead, we propose that the nucleation on  $\text{CoO}(111)$  again occurs in the form of a Lewis acid-base reaction, similar to our observation on  $\text{CoO}(100)$ . The appearance of additional IR signals in the first half cycle that do not originate from the  $-\text{NMe}_2$  ligands (neither bound to Hf nor bound to Co) indicates that follow-up reactions occur on the  $\text{CoO}(111)$  surface. In the next section, we will investigate these processes in more detail.

### 3.4. TDMAH on pristine $\text{CoO}(111)$ at 400 K.

To investigate the surface chemistry during the first half cycle, we first recorded an IR background spectrum and then pulsed small doses of TDMAH onto pristine  $\text{CoO}(111)$  at 400 K. After each pulse, we recorded an IR spectrum. The recorded spectra are shown in Figure 5a as a waterfall plot and in Figure 5b as a color plot. The evolution of the integrated peak area for signals at 3676  $\text{cm}^{-1}$ , in the CH region, at 2188  $\text{cm}^{-1}$ , and between 1630 – 1540  $\text{cm}^{-1}$  is plotted against the number of pulses in Figure 5c.

Upon dosing of TDMAH, we first observe the immediate formation of sharp bands at 3676, 2188, 1470, and 1370  $\text{cm}^{-1}$ . In addition, broad bands appear in the CH region and at around 1250 and 950  $\text{cm}^{-1}$ . From pulse 3 on, the broad bands appear as distinct signals at 2876, 2833, 2782, 1254, 952, and 910  $\text{cm}^{-1}$ . Furthermore, a broad signal develops between 1630 and 1540  $\text{cm}^{-1}$ . Upon further exposure to TDMAH, two low intensity bands appear at 1140 and 1060  $\text{cm}^{-1}$ , while the band at 1470  $\text{cm}^{-1}$  develops into a broad band. The characteristic signals (2876, 2833, 2782, 1470, 1254, 1140, 1060, and 952  $\text{cm}^{-1}$ ) and the band at 910  $\text{cm}^{-1}$  increase in intensity until saturation around pulse 60. The signals at 3676, 2188, between 1630 and 1540, and at 1370  $\text{cm}^{-1}$  first increase in intensity, reach a maximum and then decrease again. Simultaneously, the signal at 3676  $\text{cm}^{-1}$  first shifts to 3665  $\text{cm}^{-1}$  and finally transforms into a small, positive signal at 3676  $\text{cm}^{-1}$ . While the two signals at 2188 and 1370  $\text{cm}^{-1}$  disappear completely again, the broad signal at around 1600  $\text{cm}^{-1}$  only decreases in intensity and remains even after saturation. Interestingly, the bands at 2188 and around 1600  $\text{cm}^{-1}$  also reach their maximum after a different number of pulses, i.e. 8 and 14 pulses, respectively.

As discussed in the previous sections, we assign the appearance of characteristic signals to the formation of  $-\text{Hf}(\text{NMe}_2)_x$  nuclei on the surface upon exposure to TDMAH. Notably, we also observe the formation of OH groups ( $\nu(\text{OH})$  at 3676  $\text{cm}^{-1}$ ) during the formation of these nuclei. This is completely unexpected, as one would rather expect a reaction of TDMAH with defect OH that leads to the consumption and not to formation of OH species.<sup>2, 14, 48, 52-53</sup> Note that the consumption of OH species would result in a positive  $\nu(\text{OH})$  signal (observed only at a later stage of the experiment near saturation). In contrast to the nucleation experiment on CoO(100), we do not observe any shifts of the characteristic signals of the  $-\text{NMe}_2$  ligands. This observation suggests that no  $-\text{NMe}_2$  ligands are adsorbed on the CoO(111) surface. Instead, several new signals appear, the most prominent ones at 2188 and around 1600  $\text{cm}^{-1}$ .

We note that CoO(111) exhibits metallic character<sup>60</sup> and interpret the appearance of these new signals based on studies investigating the behavior of dimethylamine on Pt(111).<sup>72-74</sup> Dimethylamine has been found to dehydrogenate partially above 300 K to form methylaminocarbyne (MAC,  $\text{CNHCH}_3$ ).<sup>72, 74</sup> At 400 K, MAC further dehydrogenates leading to the formation of several different species, including methyl isocyanide (MISO,  $\text{CNCH}_3$ ) which exhibits a very characteristic  $\nu(\text{C}\equiv\text{N})$  vibration at around 2200  $\text{cm}^{-1}$ .<sup>72, 74</sup> Other proposed surface species exhibit C=N double bonds, e.g. the intermediate formimidine ( $\text{CHNMe}$ ) with  $\nu(\text{C}=\text{N})$  signals arising around 1600  $\text{cm}^{-1}$ .<sup>73</sup>

Based on this information and our observations, we suggest that TDMAH initially reacts with the CoO(111) surface via a Lewis acid-base reaction. However, the  $-\text{NMe}_2$  ligand is not stable

on CoO(111) and immediately undergoes dehydrogenation at 400 K. The hydrogen which is split off then leads to the formation of surface OH groups (giving rise to the formation of the  $\nu(\text{OH})$  band at  $3676\text{ cm}^{-1}$ ). The partial decomposition products of the ligand species with C=N double and C $\equiv$ N triple bonds give rise to the additional bands observed around 2200 and  $1600\text{ cm}^{-1}$ . In particular, we assign the band at  $2188\text{ cm}^{-1}$  to MISO binding to surface Co ions. The broad band between  $1630$  and  $1540\text{ cm}^{-1}$  probably originates from several different species with C=N double bonds, similar to the findings on Pt(111).<sup>74</sup> We note that we do not observe the characteristic  $\nu(\text{NH})$  vibration for MAC at around  $3400\text{ cm}^{-1}$ .<sup>74</sup> This suggests that at 400 K either no or only a very small amount of MAC is formed on CoO(111). Similar to the experiment on CoO(100), we tentatively assign the band at  $910\text{ cm}^{-1}$  to dehydrogenated ligands binding to surface Co ions. The ratio between the different dehydrogenated species changes over the course of the nucleation experiment as reflected by the changing ratio of the corresponding integrated peak areas. At the very beginning, the surface predominantly shows MISO species. With further exposure to TDMAH, more dehydrogenated species are formed, and the ratio gradually shifts towards species with C=N double bonds. Finally, the total amount of dehydrogenated species decreases again. Most notably, all MISO species are gradually lost, while some of the C=N double bond species remain on the surface even at saturation. Simultaneously, the previously formed OH groups on the surface are consumed again. The gradual shift of the  $\nu(\text{OH})$  band to lower wavenumbers indicates a change in the interaction with other surface species. Finally, all surface OH is consumed, including the defect OH that was present on the surface after preparation (giving rise to a small positive band at  $3676\text{ cm}^{-1}$ ). We propose two possible pathways for the consumption of OH. Firstly, TDMAH can react with acidic protons to form nuclei on the surface and volatile by-products. Secondly, the protons can react with the dehydrogenated ligands. This can lead either to the formation of less dehydrogenated species or, potentially, to their desorption. Similar to our observation on CoO(100), a comparison of the evolution of the integrated peak area of the CH region as compared to those associated with dehydrogenated ligands reveals a change in ratio. At small exposures, the surface-bound dehydrogenated ligand signals dominate the spectrum. At large exposure, most of the surface-bound ligands are lost and the  $-\text{Hf}(\text{NMe}_2)_x$  signals dominate the spectrum. Consequently, we suggest that the stoichiometry of the  $-\text{Hf}(\text{NMe}_2)_x$  species varies over the course of the experiment, with TDMAH losing more ligands at the beginning of the ALD half cycle than at later stages.

#### 4. Conclusion

In this work, we studied ALD of HfS<sub>2</sub> from the two precursors TDMAH and D<sub>2</sub>S on two atomically defined CoO surfaces, namely CoO(100) and CoO(111), under UHV conditions. In particular, we scrutinized the nucleation mechanism and surface chemistry in the first half cycle, i.e. upon reaction of the CoO surfaces with the Hf precursor. We monitored the processes in-situ by time-resolved IRAS. Our main findings can be summarized as follows:

- (1) *ALD of HfS<sub>2</sub> on pristine CoO(100) and CoO(111)*: HfS<sub>2</sub> nucleates efficiently and can be grown by ALD on both surfaces in spite of the lack of acidic protons. The CoO(100) surface is OH-free under the growth conditions and the CoO(111) surface exposes only a very small amount of OH groups at defect sites. The self-terminating surface reactions are fast and show little change in the spectral features over several ALD cycles. During the ALD process, the surface termination reversibly switches back and forth between an amine (–NMe<sub>2</sub>) and a thiol (–SD) termination. Upon TDMAH exposure, –Hf(NMe<sub>2</sub>)<sub>x</sub> adsorbents form, giving rise to IR bands at 2872, 2830, 2780, between 1430 and 1485, 1254, 1140, 1060, and 954 cm<sup>-1</sup> for CoO(100) and at 2876, 2833, 2782, 1470, 1254, 1140, 1060, and 952 cm<sup>-1</sup> for CoO(111). Upon exposure to D<sub>2</sub>S, the –NMe<sub>2</sub> ligands are cleaved and leave the surface as volatile HNMe<sub>2</sub>. However, the spectra during the first half cycle differ from those in later cycles for both ALD on CoO(100) and CoO(111), indicating that the surface chemistry in the nucleation steps differs from the growth steps.
- (2) *Nucleation mechanism on CoO(100)*: Due to the lack of acidic protons, the nucleation process occurs in the form of a Lewis acid-base reaction. As a result, –Hf(NMe<sub>2</sub>)<sub>x</sub> adsorbents bind to the surface oxygen ions and –NMe<sub>2</sub> adsorbents bind to the surface cobalt ions. During first ALD half cycle, the stoichiometry of the Hf nuclei changes drastically. At the beginning of the half cycle, TDMAH loses most of its ligands during adsorption. As the nucleation progresses, the number of ligands per Hf center gradually increases until the half cycle is completed. The process is schematically depicted in Figure 6a.
- (3) *Nucleation processes on CoO(111)*: The nucleation on CoO(111) involves a Lewis acid-base reaction followed up by a complex sequence of surface reactions of the ligands. In contrast to the reaction on CoO(100), the cleaved ligands undergo dehydrogenation reactions. These reactions lead to the formation of surface OH groups and several surface species with C=N double or C≡N triple bonds. The C≡N triple bond species is primarily associated with methyl isocyanide (MISO). The C=N double bond residues are a mixture of several species and cannot be identified in detail. During the early stages

of nucleation, TDMAH loses most of its ligands. During later stages of the nucleation process, the stoichiometry of the Hf nuclei gradually changes and TDMAH loses fewer ligands. The formed OH are eventually consumed and the MISO are displaced from the surface, while the C=N double bond species are only lost partially. Near saturation, the surface is OH free (with also the defect OH groups being consumed). The process is schematically shown in Figure 6b, where the C=N double bond species are exemplified as formimidines.

### **Acknowledgements**

This work was supported by the FAU Competence Center Engineering of Advanced Materials at the Friedrich-Alexander-Universität Erlangen-Nürnberg.

## References

1. Dasgupta, N. P.; Jung, H. J.; Trejo, O.; McDowell, M. T.; Hryciw, A.; Brongersma, M.; Sinclair, R.; Prinz, F. B. Atomic Layer Deposition of Lead Sulfide Quantum Dots on Nanowire Surfaces. *Nano Lett.* **2011**, *11*, 934-940.
2. Lu, J.; Elam, J. W.; Stair, P. C. Atomic Layer Deposition—Sequential Self-Limiting Surface Reactions for Advanced Catalyst “Bottom-up” Synthesis. *Surf. Sci. Rep.* **2016**, *71*, 410-472.
3. Knisley, T. J.; Kalutarage, L. C.; Winter, C. H. Precursors and Chemistry for the Atomic Layer Deposition of Metallic First Row Transition Metal Films. *Coord. Chem. Rev.* **2013**, *257*, 3222-3231.
4. Tiznado, H.; Bouman, M.; Kang, B.-C.; Lee, I.; Zaera, F. Mechanistic Details of Atomic Layer Deposition (ALD) Processes for Metal Nitride Film Growth. *J. Mol. Catal. A: Chem.* **2008**, *281*, 35-43.
5. Potts, S. E.; Keuning, W.; Langereis, E.; Dingemans, G.; Van de Sanden, M. C. M.; Kessels, W. M. M. Low Temperature Plasma-Enhanced Atomic Layer Deposition of Metal Oxide Thin Films. *J. Electrochem. Soc.* **2010**, *157*, P66.
6. Johnson, R. W.; Hultqvist, A.; Bent, S. F. A Brief Review of Atomic Layer Deposition: From Fundamentals to Applications. *Mater. Today* **2014**, *17*, 236-246.
7. Tan, L. K.; Liu, B.; Teng, J. H.; Guo, S.; Low, H. Y.; Loh, K. P. Atomic Layer Deposition of a MoS<sub>2</sub> Film. *Nanoscale* **2014**, *6*, 10584-10588.
8. Elam, J. W.; Schuisky, M.; Ferguson, J. D.; George, S. M. Surface Chemistry and Film Growth During Tin Atomic Layer Deposition Using TDMAT and NH<sub>3</sub>. *Thin Solid Films* **2003**, *436*, 145-156.
9. Dingemans, G.; Kessels, W. M. M. Status and Prospects of Al<sub>2</sub>O<sub>3</sub>-Based Surface Passivation Schemes for Silicon Solar Cells. *J. Vac. Sci. Technol., A* **2012**, *30*, 040802.
10. Rayner Jr., G. B.; George, S. M. Nucleation and Growth of Tantalum Nitride Atomic Layer Deposition on Al<sub>2</sub>O<sub>3</sub> Using TBDEET and Hydrogen Radicals. *J. Vac. Sci. Technol., A* **2009**, *27*, 716-724.
11. Hämäläinen, J.; Mattinen, M.; Mizohata, K.; Meinander, K.; Vehkamäki, M.; Räisänen, J.; Ritala, M.; Leskelä, M. Atomic Layer Deposition of Rhenium Disulfide. *Adv. Mater.* **2018**, *30*, 1703622.
12. Kim, H.; McIntyre, P. C. Atomic Layer Deposition of Ultrathin Metal-Oxide Films for Nano-Scale Device Applications. *J. Korean Phys. Soc.* **2006**, *48*, 5-17.
13. Groner, M. D.; Elam, J. W.; Fabreguette, F. H.; George, S. M. Electrical Characterization of Thin Al<sub>2</sub>O<sub>3</sub> Films Grown by Atomic Layer Deposition on Silicon and Various Metal Substrates. *Thin Solid Films* **2002**, *413*, 186-197.
14. George, S. M. Atomic Layer Deposition: An Overview. *Chem. Rev.* **2010**, *110*, 111-131.
15. Weber, M.; Julbe, A.; Ayril, A.; Miele, P.; Bechelany, M. Atomic Layer Deposition for Membranes: Basics, Challenges, and Opportunities. *Chem. Mater.* **2018**, *30*, 7368-7390.
16. Mackus, A. J. M.; Merckx, M. J. M.; Kessels, W. M. M. From the Bottom-Up: Toward Area-Selective Atomic Layer Deposition with High Selectivity. *Chem. Mater.* **2019**, *31*, 2-12.
17. Yang, J.; Xing, Y.; Wu, Z.; Huang, P.; Liu, L. Ultrathin Molybdenum Disulfide (MoS<sub>2</sub>) Film Obtained in Atomic Layer Deposition: A Mini-Review. *Sci. China Technol. Sci.* **2021**, *64*, 2347-2359.
18. Seo, S.; Jeong, S.; Park, H.; Shin, H.; Park, N.-G. Atomic Layer Deposition for Efficient and Stable Perovskite Solar Cells. *Chem. Comm.* **2019**, *55*, 2403-2416.
19. Tynell, T.; Karppinen, M. Atomic Layer Deposition of ZnO: A Review. *Semicond. Sci. Technol.* **2014**, *29*, 043001.
20. Cremers, V.; Puurunen, R. L.; Dendooven, J. Conformality in Atomic Layer Deposition: Current Status Overview of Analysis and Modelling. *Appl. Phys. Rev.* **2019**, *6*, 021302.
21. Oviroh, P. O.; Akbarzadeh, R.; Pan, D.; Coetsee, R. A. M.; Jen, T.-C. New Development of Atomic Layer Deposition: Processes, Methods and Applications. *Sci. Technol. Adv. Mater.* **2019**, *20*, 465-496.
22. Leskelä, M.; Ritala, M. Atomic Layer Deposition (ALD): From Precursors to Thin Film Structures. *Thin Solid Films* **2002**, *409*, 138-146.
23. Mackus, A. J. M.; Schneider, J. R.; Maclsaac, C.; Baker, J. G.; Bent, S. F. Synthesis of Doped, Ternary, and Quaternary Materials by Atomic Layer Deposition: A Review. *Chem. Mater.* **2019**, *31*, 1142-1183.
24. Bernal-Ramos, K.; Saly, M. J.; Kanjolia, R. K.; Chabal, Y. J. Atomic Layer Deposition of Cobalt Silicide Thin Films Studied by in Situ Infrared Spectroscopy. *Chem. Mater.* **2015**, *27*, 4943-4949.

25. Miikkulainen, V.; Leskelä, M.; Ritala, M.; Puurunen, R. L. Crystallinity of Inorganic Films Grown by Atomic Layer Deposition: Overview and General Trends. *J. Appl. Phys.* **2013**, *113*, 021301.
26. Motin, M. A.; Zaera, F. Thermal Chemistry of Nickel Diketonate Atomic Layer Deposition (ALD) Precursors on Tantalum and Silicon Oxide Surfaces. *J. Phys. Chem. C* **2021**, *125*, 22006-22022.
27. Chen, B.; Qin, X.; Lien, C.; Bouman, M.; Konh, M.; Duan, Y.; Teplyakov, A. V.; Zaera, F. Thermal Chemistry of Metal Organic Compounds Adsorbed on Oxide Surfaces. *Organometallics* **2020**, *39*, 928-940.
28. Oh, I.-K.; Sandoval, T. E.; Liu, T.-L.; Richey, N. E.; Nguyen, C. T.; Gu, B.; Lee, H.-B.-R.; Tonner-Zech, R.; Bent, S. F. Elucidating the Reaction Mechanism of Atomic Layer Deposition of Al<sub>2</sub>O<sub>3</sub> with a Series of Al(CH<sub>3</sub>)<sub>x</sub>Cl<sub>3-x</sub> and Al(C<sub>y</sub>H<sub>2y+1</sub>)<sub>3</sub> Precursors. *J. Am. Chem. Soc.* **2022**, *144*, 11757-11766.
29. Cabrera, W.; Halls, M. D.; Povey, I. M.; Chabal, Y. J. Surface Oxide Characterization and Interface Evolution in Atomic Layer Deposition of Al<sub>2</sub>O<sub>3</sub> on InP(100) Studied by in Situ Infrared Spectroscopy. *J. Phys. Chem. C* **2014**, *118*, 5862-5871.
30. Raiford, J. A.; Oyakhire, S. T.; Bent, S. F. Applications of Atomic Layer Deposition and Chemical Vapor Deposition for Perovskite Solar Cells. *Energy Environ. Sci.* **2020**, *13*, 1997-2023.
31. Chaves, A.; Azadani, J. G.; Alsalman, H.; da Costa, D. R.; Frisenda, R.; Chaves, A. J.; Song, S. H.; Kim, Y. D.; He, D. W.; Zhou, J. D., et al. Bandgap Engineering of Two-Dimensional Semiconductor Materials. *npj 2D Mater. Appl.* **2020**, *4*, 29.
32. Woods-Robinson, R.; Han, Y.; Zhang, H.; Ablekim, T.; Khan, I.; Persson, K. A.; Zakutayev, A. Wide Band Gap Chalcogenide Semiconductors. *Chem. Rev.* **2020**, *120*, 4007-4055.
33. Liu, R.; Wang, F.; Liu, L.; He, X.; Chen, J.; Li, Y.; Zhai, T. Band Alignment Engineering in Two-Dimensional Transition Metal Dichalcogenide-Based Heterostructures for Photodetectors. *Small Struct.* **2021**, *2*, 2000136.
34. Biyikli, N.; Haider, A. Atomic Layer Deposition: An Enabling Technology for the Growth of Functional Nanoscale Semiconductors. *Semicond. Sci. Technol.* **2017**, *32*, 093002.
35. Mattinen, M.; Leskelä, M.; Ritala, M. Atomic Layer Deposition of 2D Metal Dichalcogenides for Electronics, Catalysis, Energy Storage, and Beyond. *Adv. Mater. Interfaces* **2021**, *8*, 2001677.
36. Cao, Y.; Wähler, T.; Park, H.; Will, J.; Prihoda, A.; Moses Badlyan, N.; Fromm, L.; Yokosawa, T.; Wang, B.; Guldi, D. M., et al. Area-Selective Growth of HfS<sub>2</sub> Thin Films Via Atomic Layer Deposition at Low Temperature. *Adv. Mater. Interfaces* **2020**, *7*, 2001493.
37. Cabral Jr., C.; Lavoie, C.; Murray, C.; Pyzyna, A.; Rodbell, K. Thin Film Deposition Research and Its Impact on Microelectronics Scaling. *J. Vac. Sci. Technol., A* **2020**, *38*, 040803.
38. Huang, L.; Krasnok, A.; Alú, A.; Yu, Y.; Neshev, D.; Miroschnichenko, A. E. Enhanced Light-Matter Interaction in Two-Dimensional Transition Metal Dichalcogenides. *Rep. Prog. Phys.* **2022**, *85*, 046401.
39. Gong, C.; Zhang, Y.; Chen, W.; Chu, J.; Lei, T.; Pu, J.; Dai, L.; Wu, C.; Cheng, Y.; Zhai, T., et al. Electronic and Optoelectronic Applications Based on 2D Novel Anisotropic Transition Metal Dichalcogenides. *Adv. Sci.* **2017**, *4*, 1700231.
40. Kang, S.; Lee, D.; Kim, J.; Capasso, A.; Kang, H. S.; Park, J.-W.; Lee, C.-H.; Lee, G.-H. 2D Semiconducting Materials for Electronic and Optoelectronic Applications: Potential and Challenge. *2D Mater.* **2020**, *7*, 022003.
41. Das, S.; Pandey, D.; Thomas, J.; Roy, T. The Role of Graphene and Other 2D Materials in Solar Photovoltaics. *Adv. Mater.* **2019**, *31*, 1802722.
42. Fiori, G.; Bonaccorso, F.; Iannaccone, G.; Palacios, T.; Neumaier, D.; Seabaugh, A.; Banerjee, S. K.; Colombo, L. Electronics Based on Two-Dimensional Materials. *Nat. Nanotechnol.* **2014**, *9*, 768-779.
43. Kanazawa, T.; Amemiya, T.; Ishikawa, A.; Upadhyaya, V.; Tsuruta, K.; Tanaka, T.; Miyamoto, Y. Few-Layer HfS<sub>2</sub> Transistors. *Sci. Rep.* **2016**, *6*, 22277.
44. Fu, L.; Wang, F.; Wu, B.; Wu, N.; Huang, W.; Wang, H.; Jin, C.; Zhuang, L.; He, J.; Fu, L., et al. Van Der Waals Epitaxial Growth of Atomic Layered HfS<sub>2</sub> Crystals for Ultrasensitive Near-Infrared Phototransistors. *Adv. Mater.* **2017**, *29*, 1700439.
45. Zhang, W.; Huang, Z.; Zhang, W.; Li, Y. Two-Dimensional Semiconductors with Possible High Room Temperature Mobility. *Nano Res.* **2014**, *7*, 1731-1737.

46. Radisavljevic, B.; Radenovic, A.; Brivio, J.; Giacometti, V.; Kis, A. Single-Layer MoS<sub>2</sub> Transistors. *Nat. Nanotechnol.* **2011**, *6*, 147-150.
47. Radisavljevic, B.; Kis, A. Mobility Engineering and a Metal–Insulator Transition in Monolayer MoS<sub>2</sub>. *Nat. Mater.* **2013**, *12*, 815-820.
48. Killampalli, A. S.; Ma, P. F.; Engstrom, J. R. The Reaction of Tetrakis(Dimethylamido)Titanium with Self-Assembled Alkyltrichlorosilane Monolayers Possessing –OH, –NH<sub>2</sub>, and –CH<sub>3</sub> Terminal Groups. *J. Am. Chem. Soc.* **2005**, *127*, 6300-6310.
49. Dube, A.; Sharma, M.; Ma, P. F.; Engstrom, J. R. Effects of Interfacial Organic Layers on Thin Film Nucleation in Atomic Layer Deposition. *Appl. Phys. Lett.* **2006**, *89*, 164108.
50. Dube, A.; Sharma, M.; Ma, P. F.; Ercius, P. A.; Muller, D. A.; Engstrom, J. R. Effects of Interfacial Organic Layers on Nucleation, Growth, and Morphological Evolution in Atomic Layer Thin Film Deposition. *J. Phys. Chem. C* **2007**, *111*, 11045-11058.
51. Li, M.; Dai, M.; Chabal, Y. J. Atomic Layer Deposition of Aluminum Oxide on Carboxylic Acid-Terminated Self-Assembled Monolayers. *Langmuir* **2009**, *25*, 1911-1914.
52. Fickenscher, G.; Steffen, J.; Görling, A.; Libuda, J. r. Atomic Layer Deposition of HfS<sub>2</sub> on Functionalized Self-Assembled Monolayers on Ordered Oxide Surfaces: A Model Study under UHV Conditions. *J. Phys. Chem. C* **2024**, *128*, 798-809.
53. Fickenscher, G.; Fromm, L.; Görling, A.; Libuda, J. Atomic Layer Deposition of HfS<sub>2</sub> on Oxide Interfaces: A Model Study on the Initial Nucleation Processes. *J. Phys. Chem. C* **2022**, *126*, 21596-21605.
54. Marichy, C.; Pinna, N. Carbon-Nanostructures Coated/Decorated by Atomic Layer Deposition: Growth and Applications. *Coord. Chem. Rev.* **2013**, *257*, 3232-3253.
55. Li, K.; Li, S.; Li, N.; Dixon, D. A.; Klein, T. M. Tetrakis(dimethylamido)hafnium Adsorption and Reaction on Hydrogen Terminated Si(100) Surfaces. *J. Phys. Chem. C* **2010**, *114*, 14061-14075.
56. Patwardhan, S.; Cao, D. H.; Schatz, G. C.; Martinson, A. B. F. Atomic Layer Deposition Nucleation on Isolated Self-Assembled Monolayer Functional Groups: A Combined DFT and Experimental Study. *ACS Appl. Energy Mater.* **2019**, *2*, 4618-4628.
57. Parsons, G. N.; Clark, R. D. Area-Selective Deposition: Fundamentals, Applications, and Future Outlook. *Chem. Mater.* **2020**, *32*, 4920-4953.
58. Färm, E.; Kemell, M.; Ritala, M.; Leskelä, M. Self-Assembled Octadecyltrimethoxysilane Monolayers Enabling Selective-Area Atomic Layer Deposition of Iridium. *Chem. Vap. Depos.* **2006**, *12*, 415-417.
59. Lee, H.-B.-R.; Bent, S. F. Formation of Continuous Pt Films on the Graphite Surface by Atomic Layer Deposition with Reactive O<sub>3</sub>. *Chem. Mater.* **2015**, *27*, 6802-6809.
60. Heinz, K.; Hammer, L. Epitaxial Cobalt Oxide Films on Ir(100)—the Importance of Crystallographic Analyses. *J. Phys.: Condens. Matter* **2013**, *25*, 173001.
61. Biedermann, K.; Gubo, M.; Hammer, L.; Heinz, K. Phases and Phase Transitions of Hexagonal Cobalt Oxide Films on Ir(100)-(1×1). *J. Phys.: Condens. Matter* **2009**, *21*, 185003.
62. Meyer, W.; Biedermann, K.; Gubo, M.; Hammer, L.; Heinz, K. Superstructure in the Termination of CoO(111) Surfaces: Low-Energy Electron Diffraction and Scanning Tunneling Microscopy. *Phys. Rev. B* **2009**, *79*, 121403.
63. Schwarz, M.; Faisal, F.; Mohr, S.; Hohner, C.; Werner, K.; Xu, T.; Skála, T.; Tsud, N.; Prince, K. C.; Matolín, V., et al. Structure-Dependent Dissociation of Water on Cobalt Oxide. *J. Phys. Chem. Lett.* **2018**, *9*, 2763-2769.
64. Schwarz, M.; Mohr, S.; Hohner, C.; Werner, K.; Xu, T.; Libuda, J. Water on Atomically-Defined Cobalt Oxide Surfaces Studied by Temperature-Programmed Ir Reflection Absorption Spectroscopy and Steady State Isotopic Exchange. *J. Phys. Chem. C* **2019**, *123*, 7673-7681.
65. Meyer, W.; Biedermann, K.; Gubo, M.; Hammer, L.; Heinz, K. Surface Structure of Polar Co<sub>3</sub>O<sub>4</sub>(111) Films Grown Epitaxially on Ir(100)-(1×1). *J. Phys.: Condens. Matter* **2008**, *20*, 265011.
66. Xu, T.; Schwarz, M.; Werner, K.; Mohr, S.; Amende, M.; Libuda, J. Structure-Dependent Anchoring of Organic Molecules to Atomically Defined Oxide Surfaces: Phthalic Acid on Co<sub>3</sub>O<sub>4</sub>(111), CoO(100), and CoO(111). *Chem. Eur. J.* **2016**, *22*, 5384-5396.

67. Mohr, S.; Schmitt, T.; Döpfer, T.; Xiang, F.; Schwarz, M.; Görling, A.; Schneider, M. A.; Libuda, J. Coverage-Dependent Anchoring of 4,4'-Biphenyl Dicarboxylic Acid to Coo(111) Thin Films. *Langmuir* **2017**, *33*, 4178-4188.
68. Xu, T.; Schwarz, M.; Werner, K.; Mohr, S.; Amende, M.; Libuda, J. The Surface Structure Matters: Thermal Stability of Phthalic Acid Anchored to Atomically-Defined Cobalt Oxide Films. *Phys. Chem. Chem. Phys.* **2016**, *18*, 10419-10427.
69. Wähler, T.; Schuster, R.; Libuda, J. Surface Structure Controls Self-Metalation: In-Situ Ir Studies of Anchored Porphyrins on Atomically-Defined Cobalt Oxide Surfaces. *J. Phys. Chem. C* **2020**, *124*, 21538-21548.
70. Schwarz, M.; Hohner, C.; Mohr, S.; Libuda, J. Dissociative Adsorption of Benzoic Acid on Well-Ordered Cobalt Oxide Surfaces: Role of the Protons. *J. Phys. Chem. C* **2017**, *121*, 28317-28327.
71. Schuschke, C.; Schwarz, M.; Hohner, C.; Silva, T. N.; Libuda, J. Phosphonic Acids on Well-Ordered Co Surfaces: The Binding Motif Depends on the Surface Structure. *J. Phys. Chem. C* **2018**, *122*, 16221-16233.
72. Eschenbacher, R.; Steffen, J.; Farrugia, K.; Taccardi, N.; Wasserscheid, P.; Görling, A.; Libuda, J. Reactivity of a Model Scill: Influence of Co-Adsorbed [C<sub>2</sub>C<sub>1</sub>im][Otf] on the Dehydrogenation of Dimethylamine on Pt(111). *Surf. Sci.* **2024**, 122453.
73. Mudiyansele, K.; Trenary, M.; Meyer, R. J. Formation of Methyl Isocyanide from Dimethylamine on Pt(111). *J. Phys. Chem. C* **2008**, *112*, 3794-3799.
74. Kang, D.-H.; Trenary, M. Surface Chemistry of Dimethylamine on Pt(111): Formation of Methylaminocarbyne and Its Decomposition Products. *Surf. Sci.* **2002**, *519*, 40-56.

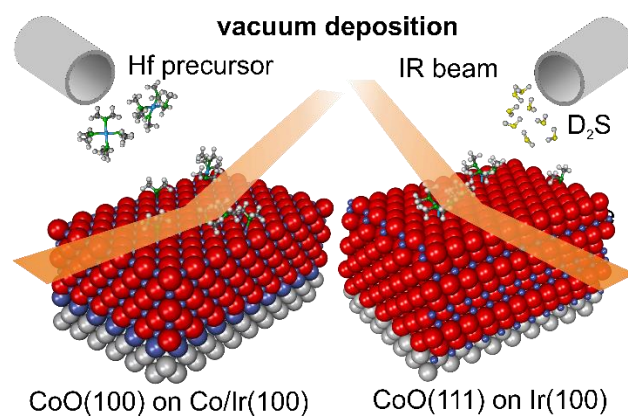
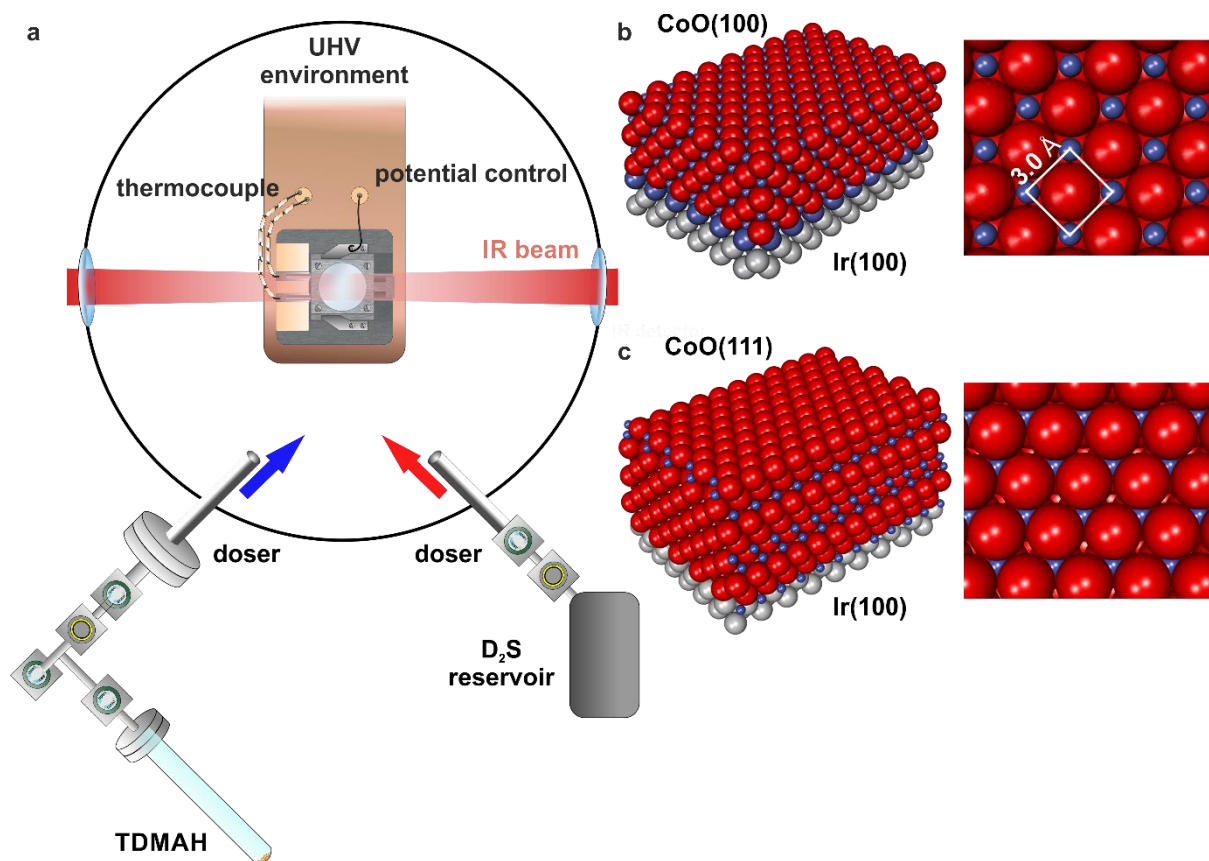
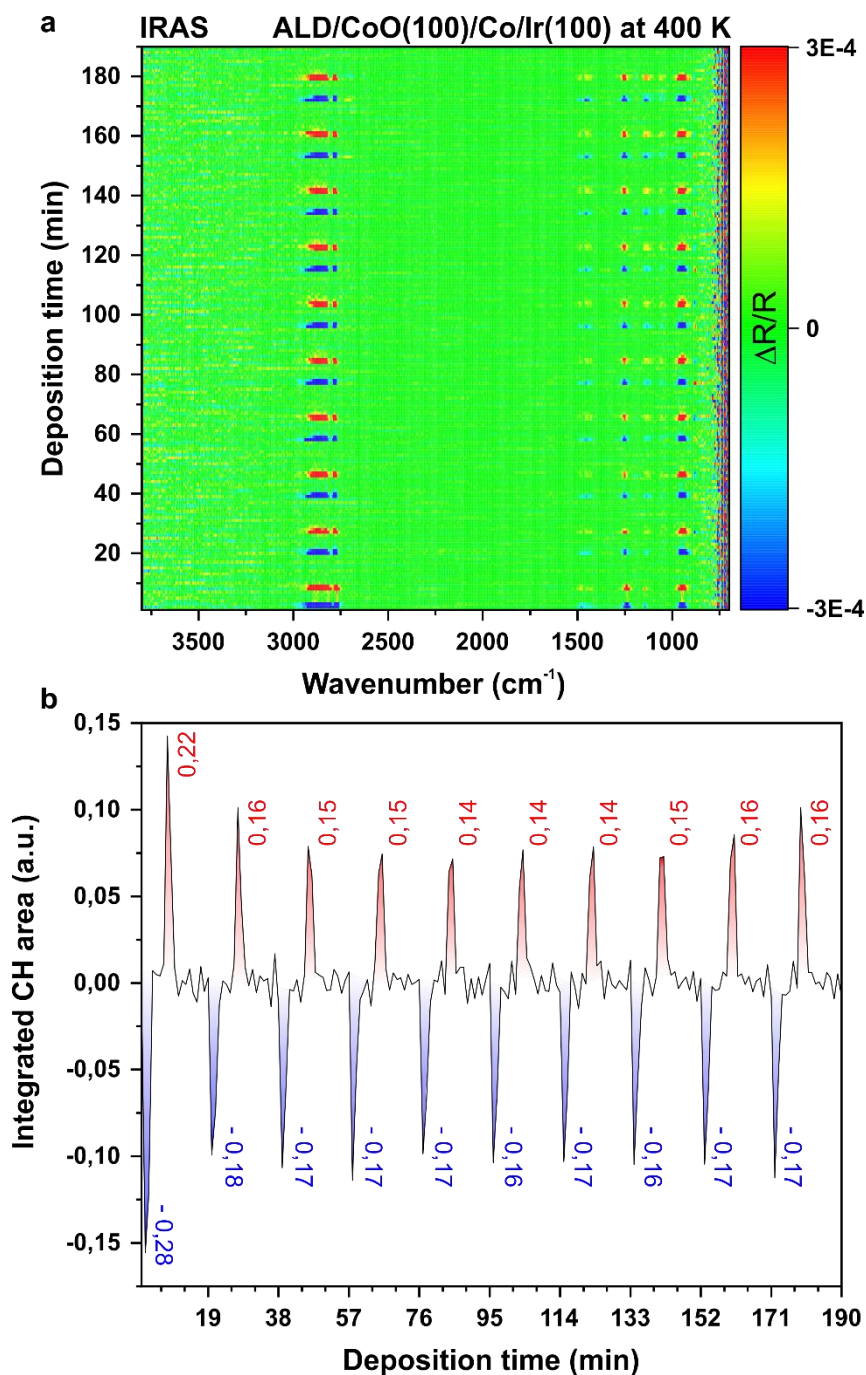


Figure TOC



**Figure 1:** a) Schematic representation of the UHV ALD experiment and in situ IRAS setup; b) ball models of the CoO(100) thin film as side and top view; c) ball models of the CoO(111) thin film as side and top view.



**Figure 2:** a) IRAS data recorded during the ALD experiment on CoO(100)/Co/Ir(100) at 400 K shown as 2D color plot in the form of difference spectra; b) Integrated signal area in the CH region as a function of deposition time, the corresponding peak area (arbitrary units) of the color-coded signals is indicated as a value next to the respective peak.

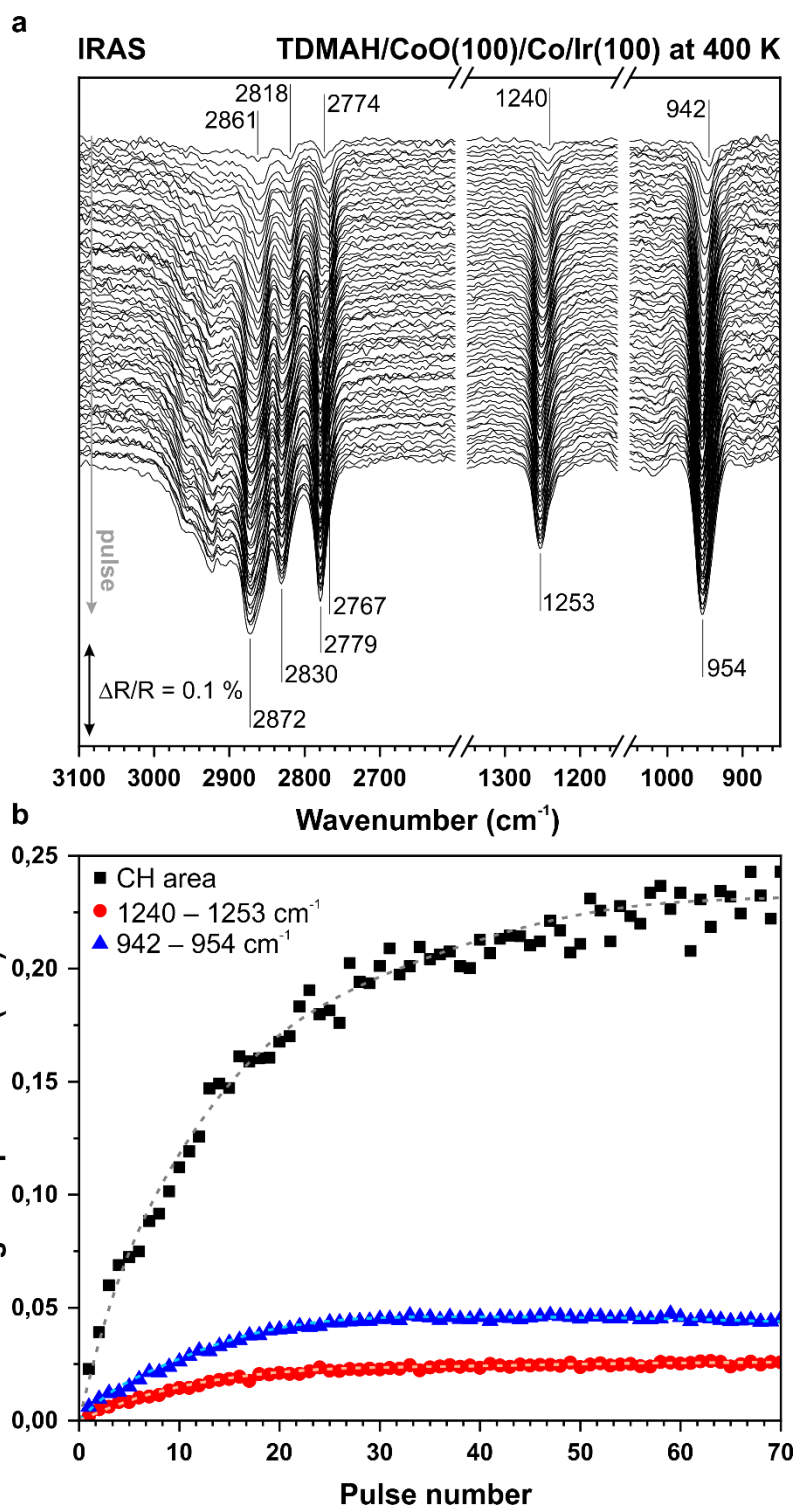


**Figure 3:** IR spectra recorded upon exposure of the pristine CoO(100) surface to small doses of TDMAH at 400 K (referenced to pristine CoO(100)); b) peak area of the signals in the CH region, 1240 – 1253 cm<sup>-1</sup> and 942 – 954 cm<sup>-1</sup> plotted as a function of pulse number.

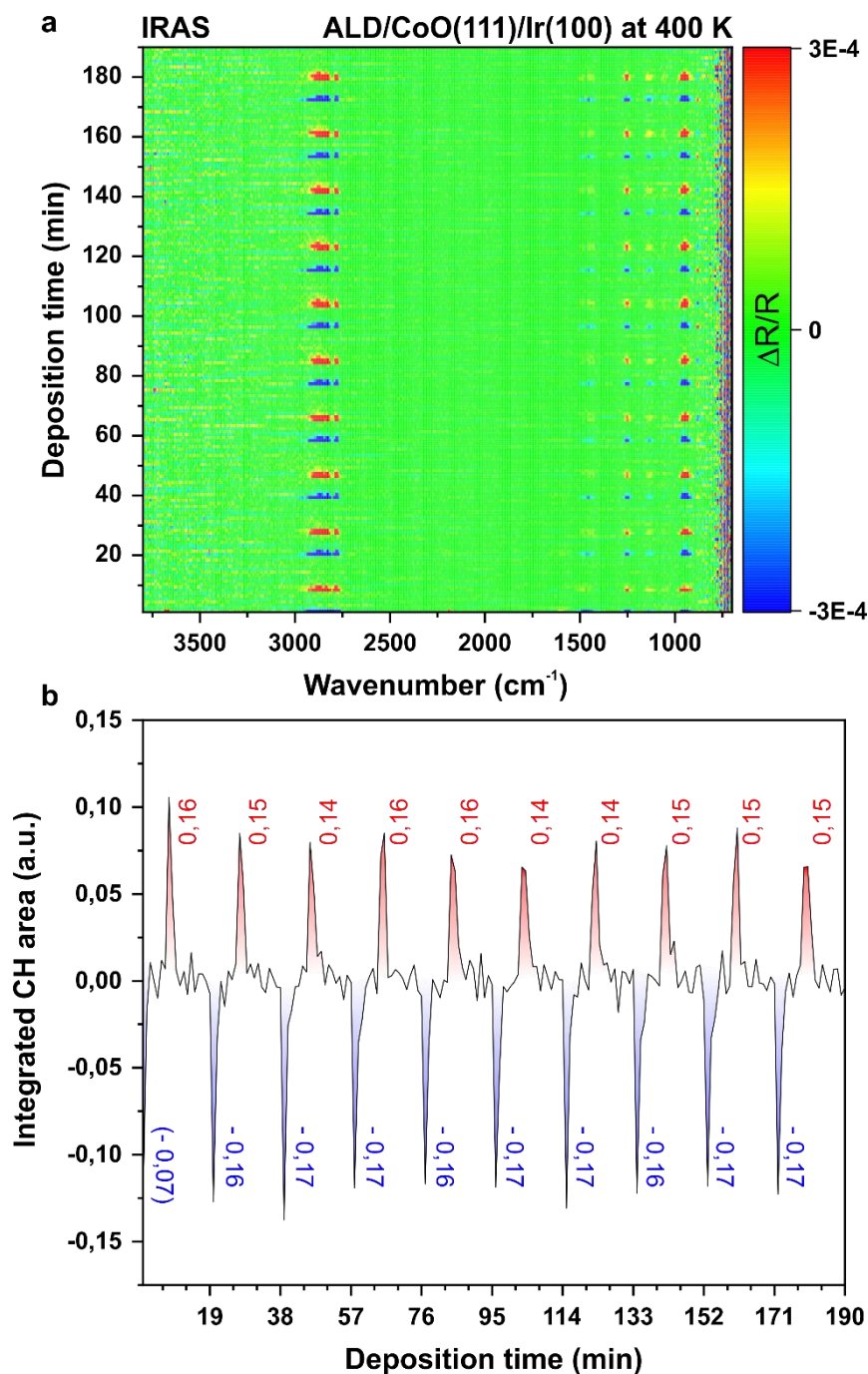


**Figure 4:** a) IRAS data recorded during the ALD experiment on CoO(111)/Ir(100) at 400 K shown as 2D color plot in the form of difference spectra; b) integrated signal area in the CH region as a function of deposition time, the corresponding peak area of the color-coded signals is indicated as a number next to the respective peak.

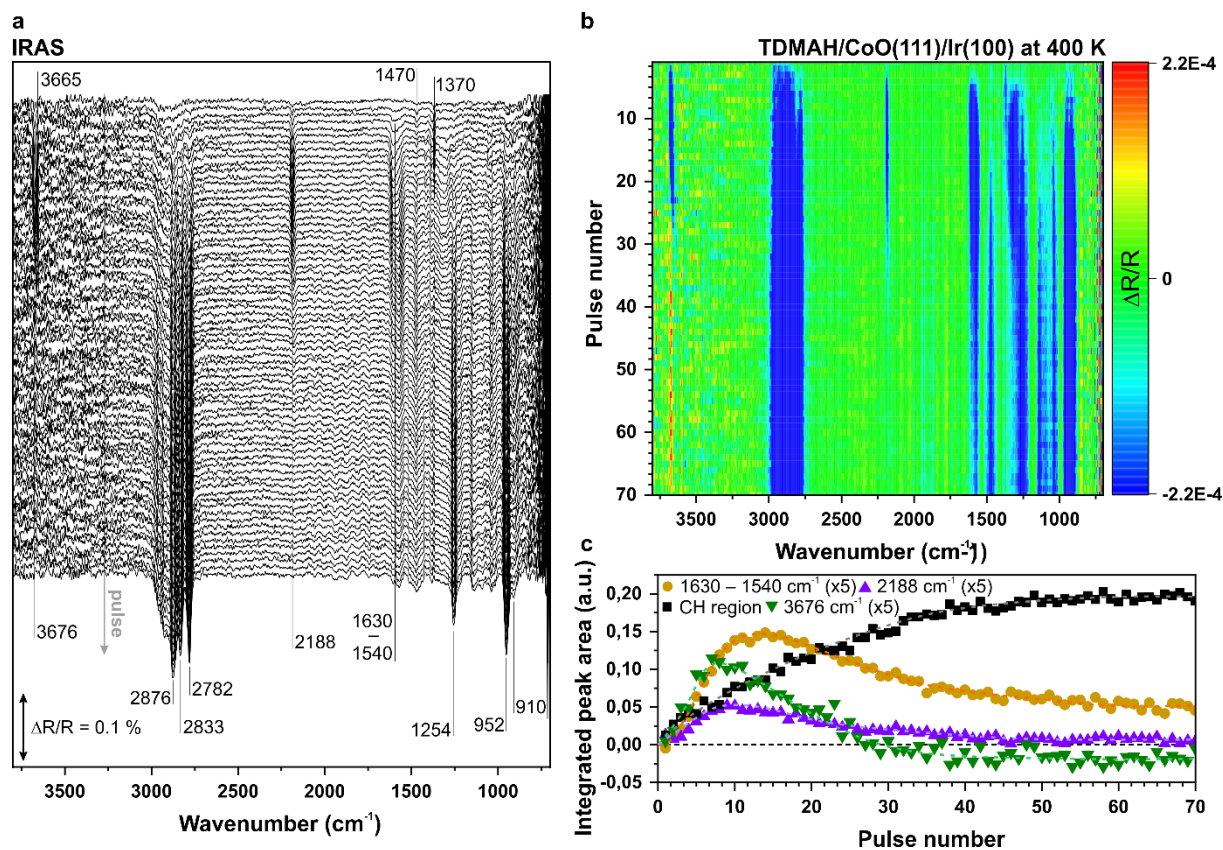


**Figure 5:** a) Waterfall plot of IR spectra recorded upon exposure of the pristine CoO(111) surface to small doses of TDMAH at 400 K (referenced to pristine CoO(111)); b) IRAS data recorded upon exposure of the pristine CoO(111) surface to small doses of TDMAH at 400 K shown as 2D color plot (referenced to pristine CoO(111)); c) peak area of signals at  $3676\text{ cm}^{-1}$ , in the CH region,  $2188\text{ cm}^{-1}$  and  $1630 - 1540\text{ cm}^{-1}$  plotted as a function of pulse number.

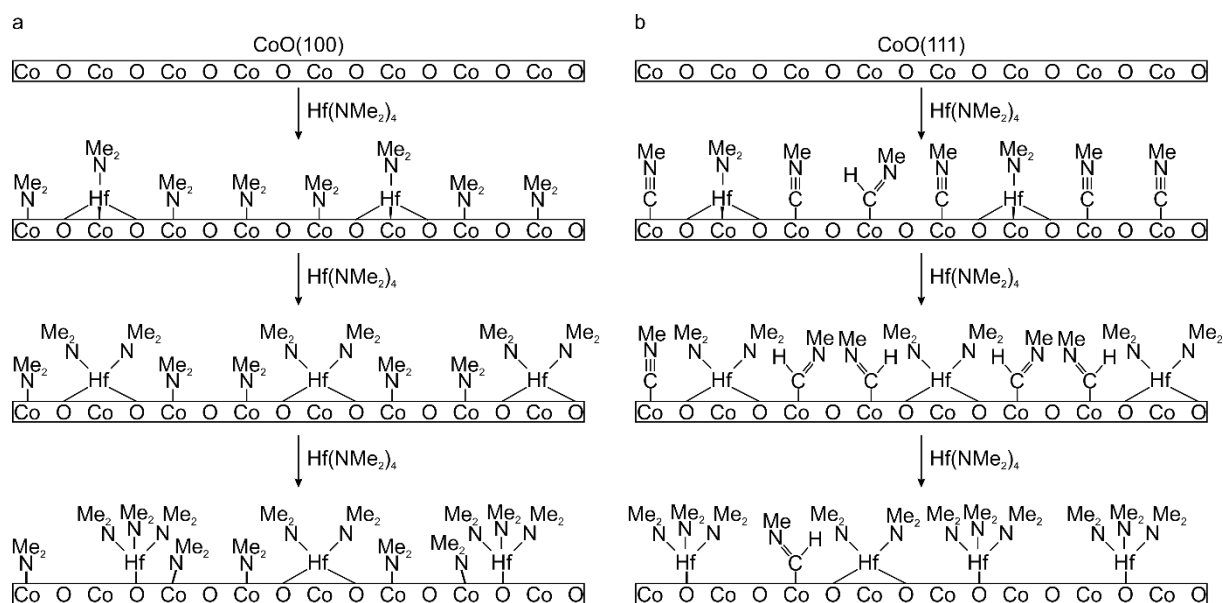


**Figure 6:** Schematic of the nucleation step and appearing surface species in the first ALD half cycle for the deposition of TDMAH on a) CoO(100) and b) CoO(111).